

# Searches for New Milky Way Satellites from the First Two Years of Data of the Subaru/Hyper Suprime-Cam Survey: Discovery of Cetus III

Daisuke Homma<sup>1</sup>, Masashi Chiba<sup>1</sup>, Sakurako Okamoto<sup>2</sup>,  
Yutaka Komiyama<sup>3,4</sup>, Masayuki Tanaka<sup>3</sup>, Mikito Tanaka<sup>1</sup>,  
Miho N. Ishigaki<sup>5</sup>, Kohei Hayashi<sup>6,5</sup>, Nobuo Arimoto<sup>7,4</sup>, José A. Garmilla<sup>8</sup>,  
Robert H. Lupton<sup>8</sup>, Michael A. Strauss<sup>8</sup>, Satoshi Miyazaki<sup>3,4</sup>,  
Shiang-Yu Wang<sup>9</sup>, and Hitoshi Murayama<sup>5</sup>

<sup>1</sup>Astronomical Institute, Tohoku University, Aoba-ku, Sendai 980-8578, Japan

<sup>2</sup>Shanghai Astronomical Observatory, 80 Nandan Road, Shanghai 200030, China

<sup>3</sup>National Astronomical Observatory of Japan, 2-21-1 Osawa, Mitaka, Tokyo 181-8588, Japan

<sup>4</sup>The Graduate University for Advanced Studies, Osawa 2-21-1, Mitaka, Tokyo 181-8588, Japan

<sup>5</sup>Kavli Institute for the Physics and Mathematics of the Universe (WPI), The University of Tokyo, Kashiwa, Chiba 277-8583, Japan

<sup>6</sup>Kavli Institute for Astronomy and Astrophysics, Peking University, Beijing 100871, China

<sup>7</sup>Subaru Telescope, National Astronomical Observatory of Japan, 650 North A'ohoku Place, Hilo, HI 96720, USA

<sup>8</sup>Princeton University Observatory, Peyton Hall, Princeton, NJ 08544, USA

<sup>9</sup>Institute of Astronomy and Astrophysics, Academia Sinica, Taipei, 10617, Taiwan

\*E-mail: chiba@astr.tohoku.ac.jp

Received (reception date); Accepted (acceptation date)

## Abstract

We present the results from a search for new Milky Way (MW) satellites from the first two years of data from the Hyper Suprime-Cam (HSC) Subaru Strategic Program (SSP)  $\sim 300$  deg<sup>2</sup> and report the discovery of an ultra-faint dwarf galaxy in Cetus. This is the second ultra-faint dwarf we have discovered after Virgo I reported in our previous paper. This new satellite, Cetus III, has been identified as a statistically significant ( $10.7\sigma$ ) spatial overdensity of star-like objects, which are selected from a relevant isochrone filter designed for a metal-poor and old stellar population. This stellar system is located at a heliocentric distance of  $251^{+24}_{-11}$  kpc with a most likely absolute magnitude of  $M_V = -2.4 \pm 0.6$  mag estimated from a Monte Carlo analysis. Cetus III is extended with a half-light radius of  $r_h = 90^{+42}_{-17}$  pc, suggesting that this is a faint dwarf satellite in the MW located beyond the detection limit of the Sloan Digital Sky Survey. We also revisit and update the parameters for Virgo I finding  $M_V = -0.33^{+0.75}_{-0.87}$  mag and  $r_h = 47^{+19}_{-13}$  pc. Using simulations of  $\Lambda$ -dominated cold dark matter models, we predict that we should find one or two new MW satellites from  $\sim 300$  deg<sup>2</sup> HSC-SSP data, in rough agreement with the discovery rate so far. The further survey and completion of HSC-SSP over  $\sim 1,400$  deg<sup>2</sup> will provide robust insights into the missing satellites problem.

**Key words:** galaxies: dwarf — galaxies: individual (Cetus III, Virgo I) — Local Group

## 1 Introduction

The current standard theory of structure formation based on  $\Lambda$ -dominated cold dark matter ( $\Lambda$ CDM) models is successful for understanding the origin and evolution of observed large-scale structures in the universe on scales larger than  $\sim 1$  Mpc (e.g., Tegmark et al. 2004). The theory states that larger dark halos are formed by the hierarchical assembly of smaller halos, where the latter formed earlier and thus have higher internal densities than the former. As a consequence, dark halos like those associated with the Milky Way (MW) are surrounded by hundreds of smaller subhalos, which survive the merging and tidal processes (Klypin et al. 1999; Moore et al. 1999). However, this prediction is in conflict with the observed number of only  $\sim 50$  MW satellites. This is the so-called missing satellites problem. The theory also has several unsolved issues on small scales, including the core/cusp problem (e.g., Moore et al. 1994; Burkert 1995; de Blok et al. 2001; Swaters et al. 2003; Gilmore et al. 2007; Oh et al. 2011), the too-big-to-fail problem (Boylan-Kolchin et al. 2011; Boylan-Kolchin et al. 2012), and the observed anisotropic distribution of MW and Andromeda satellites (e.g., Kroupa et al. 2005; McConnachie & Irwin 2006; Ibata et al. 2013; Pawlowski et al. 2012; Pawlowski et al. 2013; Pawlowski et al. 2015).

A key in these small-scale issues of dark matter is to understand the basic properties of dwarf spheroidal galaxies (dSphs) as companions of the MW and Andromeda. DSphs are faint, metal-poor, old stellar systems, similar to globular clusters, but they are extended and largely dominated by dark matter, unlike globular clusters (e.g., (Gilmore et al. 2007; Simon & Geha 2007)). Thus, dSphs play an important role as tracers of background dark matter, and their total number and spatial distribution in the MW as well as their internal density profiles set invaluable constraints on the nature of dark matter on small scales and the resultant effects on the star-formation history of dSphs (e.g., Milosavljević & Bromm 2014; Okayasu & Chiba 2016).

One of the possible solutions to the missing satellites problem is that we still are undercounting the population of dwarf satellites in the MW due to various observational biases (Koposov et al. 2008; Tollerud et al. 2008). In particular, searches for new dSphs are generally limited in survey area and depth. To overcome this limitation, several survey programs have been undertaken to find new dwarf satellites in the MW, including the Sloan Digital Sky Survey (SDSS) (York et al. 2000), the Dark Energy Survey (DES) (Abbott et al. 2016), the Pan-STARRS 1 (PS1)  $3\pi$  survey (Chambers et al. 2016), which have revealed a number of new ultra-faint dwarf galax-

ies (UFDs) with  $V$ -band absolute magnitude,  $M_V$ , fainter than  $-8$  mag (e.g., Willman et al. 2005; Sakamoto & Hasegawa 2006; Belokurov et al. 2006; Laevens et al. 2014; Kim et al. 2015; Kim & Jerjen 2015; Laevens et al. 2015a; Laevens et al. 2015b; Bechtol et al. 2015; Koposov et al. 2015; Drlica-Wagner et al. 2015). It is thus expected that still more dwarf satellites remain undetected in the outskirts of the MW because of their faint magnitudes and large distances.

This paper presents our second discovery of a new faint dwarf satellite in the MW from the ongoing Subaru Strategic Program (SSP) using Hyper Suprime-Cam (HSC) (see for the details of HSC-SSP, Aihara et al. 2017a; Aihara et al. 2017b). HSC is a prime-focus camera on Subaru with a 1.5 deg diameter field of view (Miyazaki et al. 2012; Miyazaki et al. 2017). Our team has already reported the discovery of a new UFD, Virgo I, from the early data of HSC-SSP (Homma et al. 2016). In this paper, we refine and update our method for the search of new dwarf satellites based on the analysis of statistically significant spatial overdensities from HSC-SSP data, as presented in Section 2. Section 3 is devoted to the results of our algorithm for detecting new satellites, which reveals a new candidate in the direction of Cetus, named Cetus III. The structural parameters of Cetus III as well as its heliocentric distance and  $V$ -band absolute magnitude are also derived. In Section 4, we examine the significance of having found these two UFDs from the early HSC data and predict how many more UFDs would be found in the survey program. Finally, our conclusions are presented in Section 5.

## 2 Data and Method

We utilize the imaging data of HSC-SSP survey in its Wide layer, which is aiming to observe  $\sim 1,400$  deg<sup>2</sup> in five photometric bands ( $g$ ,  $r$ ,  $i$ ,  $z$ , and  $y$ ) (for details, see Aihara et al. 2017a; Aihara et al. 2017b). The target  $5\sigma$  point-source limiting magnitudes in this layer are ( $g$ ,  $r$ ,  $i$ ,  $z$ ,  $y$ ) = (26.5, 26.1, 25.9, 25.1, 24.4) mag. In this paper, we use the  $g$ ,  $r$ , and  $i$ -band data obtained before 2016 April (internal data release S16A), covering  $\sim 300$  deg<sup>2</sup> in 6 fields along the celestial equator (named XMM, WIDE12H, WIDE01H, VVDS, GAMA15H, and GAMA09H) as well as one field around (RA,DEC)=( $242^\circ$ ,  $43^\circ$ ) (HECTOMAP). For WIDE01H, only  $g$  and  $r$ -band data are available in S16A. The HSC data are processed with hscPipe v4.0.2 (Bosch et al. 2017), a branch of the Large Synoptic Survey Telescope pipeline (Ivezic et al. 2008; Axelrod et al. 2010; Juric et al. 2015) calibrated against

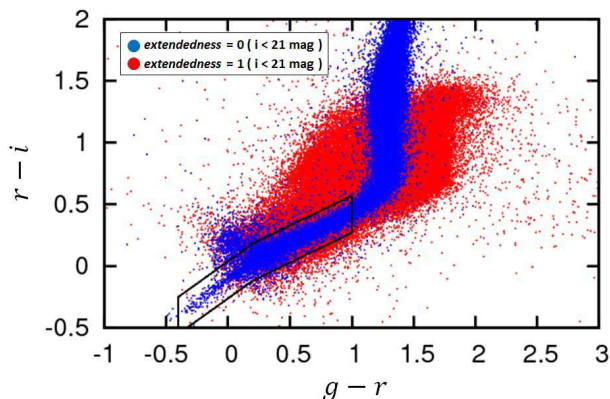


**Fig. 1.** Color-color diagram of bright sources with  $i < 21$  mag in WIDE12H. Blue and red dots denote point sources ( $extendedness=0$ ) and galaxies ( $extendedness=1$ ), respectively. The polygon outlines the color cut we use for the selection of target stars in the MW halo.

Pan-STARRS1 photometry and astrometry (Schlafly et al. 2012; Tonry et al. 2012; Magnier et al. 2013). All the photometry data are corrected for the mean Galactic foreground extinction,  $A_V$  (Schlafly & Finkbeiner 2011). We note that most of the dust should be closer than the UFDs we are looking for.

## 2.1 Selection of target stars

For the purpose of searching efficiently for new faint satellites in the MW halo, we select stars from the HSC data as follows: (1) their images are point-like to avoid galaxies, (2) their  $g-r$  colors are bluer than 1 to eliminate foreground M-type disk stars, and (3) their  $g-r$  vs.  $r-i$  colors follow the fiducial relation expected for stars to remove the remaining contaminants.

First, to select point sources, we adopt the *extendedness* parameter from the pipeline following our previous paper (Homma et al. 2016). In brief, this parameter is computed based on the ratio between PSF and cmodel fluxes (Abazajian et al. 2004), where a point source has this ratio larger than 0.985. We use this parameter measured in the  $i$ -band, in which the seeing is typically the best of our five filters with a median of about  $0''.6$ . As detailed in Aihara et al. (2017a), using the combination of the HSC COSMOS and HST/ACS data (Leauthaud et al. 2007), the completeness and contamination of this star/galaxy classification is defined and quantified as follows. The completeness, defined as the fraction of objects that are classified as stars by ACS, and correctly classified as stars by HSC, is above 90% at  $i < 22.5$ , and drops to  $\sim 50\%$  at  $i = 24.5$ . The contamination, defined as the fraction of HSC-classified stars which are classified as galaxies by ACS, is close to zero at  $i < 23$ , but increases to  $\sim 50\%$  at  $i = 24.5$ . In this work, we adopt the *extendedness* parameter down to  $i = 24.5$  to select stars.

We then use the color data to eliminate the remaining contaminants, including foreground disk stars and background quasars and compact galaxies, which remain after the *extend-*

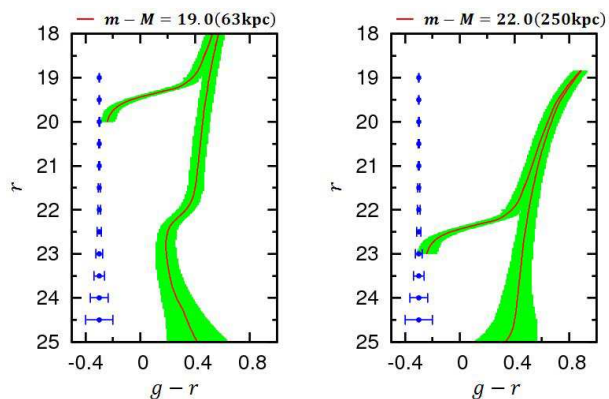


**Fig. 2.** Example of a CMD filter (green shaded area) including an isochrone (red line) for an old, metal-poor system [age of 13 Gyr and metallicity of  $[M/H] = -2.2$ ] at a distance of 63 kpc (left) and 250 kpc (right panel), respectively. The error bars show a typical measurement error in color at each  $r$  magnitude.

*edness* cut. For this purpose, we plot, in Figure 1, the  $g-r$  vs.  $r-i$  relation for both stars ( $extendedness=0$ ) and galaxies ( $extendedness=1$ ) in the WIDE12H field with brightness of  $i < 21$  mag, where star/galaxy classification is very reliable. As is clear, star-like objects show a narrow, characteristic sequence in this color-color diagram compared to galaxies. Thus to optimize the selection of stars further from the sample of point sources with  $extendedness=0$ , we set a color cut based on this color-color diagram, as has been done in previous work (e.g., Willman et al. 2002). Namely, we first eliminate the numerous red-color stars with  $g-r \geq 1$  in Figure 1, which are dominated by M-type stars in the MW disk. Then, as most likely star candidates in the MW halo, we select point sources inside a polygon in the diagram, which is bounded by  $(g-r, r-i) = (1.00, 0.27)$ ,  $(1.00, 0.57)$ ,  $(-0.4, -0.55)$ , and  $(-0.4, -0.25)$ . We note that the width of this color cut in  $r-i$ , 0.3 mag, is wider than the typical photometric error of  $r-i$  at  $i = 24.5$ , so as to optimally include candidate stars in the MW halo. Although this color cut is not perfect in removing all the quasars and galaxies, we adopt point sources selected from this color cut to search for any signatures of overdensities as described in the next subsection.

## 2.2 Detection algorithm for stellar overdensities

Our targets here are old, metal-poor stellar systems at a particular distance, which reveal their presence as statistically significant spatial overdensities relative to the foreground and background noise from MW stars and distant galaxies/quasars. For this purpose, we adopt the algorithm below, following several other works (Koposov et al. 2008; Walsh et al. 2009).

### 2.2.1 Isochrone filter

Ultra-faint dwarf satellites discovered so far show a characteristic locus in the color-magnitude (CMD) diagram, which is simi-

lar to that of an old MW globular cluster, namely an old, metal-poor stellar system. Thus to enhance the clustering signal of stars in a satellite over the background noise, we select stars which are included within a CMD locus defined for an old stellar population within a particular distance range from the Sun. This isochrone filter is made based on a PARSEC isochrone (Bressan et al. 2012), in which we assume an age of 13 Gyr and metallicity of  $z = 0.0001$  ( $[M/H] = -2.2$ ). We adopt a CMD defined with  $g-r$  vs.  $r$ -band absolute magnitude,  $M_r$ , and convert the SDSS filter system available for the PARSEC isochrone to the current HSC filter system,  $g = g_{\text{SDSS}} - a(g_{\text{SDSS}} - r_{\text{SDSS}}) - b$  and  $r = r_{\text{SDSS}} - c(r_{\text{SDSS}} - i_{\text{SDSS}}) - d$ , where  $(a, b, c, d) = (0.074, 0.011, 0.004, 0.001)$  and the subscript SDSS denotes the SDSS system (Homma et al. 2016).

We then set the finite width for the selection filter as a function of  $r$ -band magnitude, which is the quadrature sum of a  $1\sigma$  ( $g-r$ ) color measurement error in HSC imaging and a typical color dispersion of about  $\pm 0.05$  mag at the location of the RGB arising from a metallicity dispersion of  $\pm 0.5$  dex, which is typically found in dSphs. We shift this isochrone filter over distance moduli of  $(m-M)_0 = 16.5$  to 24.0 in 0.5 mag steps, which corresponds to searching for old stellar systems with the heliocentric distance,  $D_\odot$ , between 20 kpc and 631 kpc.

Figure 2 shows two examples of a CMD isochrone filter placed at  $(m-M)_0 = 19.0$  ( $D_\odot = 63$  kpc) and  $(m-M)_0 = 22.0$  (250 kpc). In the former case for a relatively nearby stellar system, it is possible to detect the CMD feature near the main sequence turn-off, whereas the latter more distant system shows only a red giant branch and horizontal branch features.

### 2.2.2 Search for overdensities and their statistical significance

After selecting stars using the above isochrone filter at each distance, we search for the signature of their spatial overdensities and examine their statistical significance. We count selected stars in  $0^\circ.05 \times 0^\circ.05$  bins in right ascension and declination, with an overlap of  $0^\circ.025$  in each direction. Here, the grid interval of  $0^\circ.05$  corresponds to a typical half-light diameter ( $\sim 80$  pc) of an ultra-faint dwarf galaxy at a distance of 90 kpc, and any signature of dwarf galaxy at and beyond this distance, which is our target with HSC, can be detected within this grid interval.

We count the number of stars at each cell,  $n_{i,j}$ , where if a cell contains no stars,  $n_{i,j} = 0$ , e.g. due to masking in the vicinity of a bright-star image, we just ignore it for the following calculation. We then calculate the mean density ( $\bar{n}$ ) and its dispersion ( $\sigma$ ) over all cells for each of the Wide layer fields separately and define the normalized signal in each cell,  $S_{i,j}$ , giving the number of standard deviations above the local mean (e.g., Koposov et al. 2008; Walsh et al. 2009),

$$S_{i,j} = \frac{n_{i,j} - \bar{n}}{\sigma}. \quad (1)$$

We find that the distribution of  $S$  is almost Gaussian.

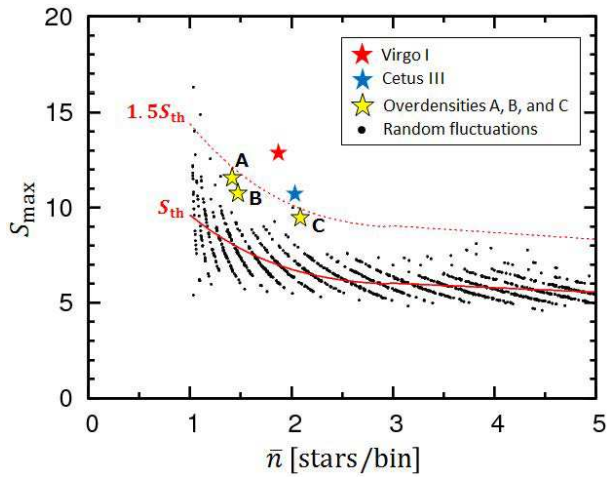
In order to find candidate overdensities that are statistically high enough to reject false detections, it is necessary to set detection thresholds for the value of  $S$  (Walsh et al. 2009). For this purpose, we obtain the characteristic distribution of  $S$  for purely random fluctuations in stellar densities as follows. First, we define an area with  $\Delta\text{RA} = 10$  deg and  $\Delta\text{DEC} = 5$  deg in each of the HSC Wide-layer survey fields (corresponding to the typical survey area of  $\sim 50$  deg<sup>2</sup>). In each field, stars are randomly distributed to reproduce the mean number density,  $\bar{n}$ , by counting stars in each cell; again we ignore cells with no stars  $n_{i,j} = 0$  in the calculation. We then estimate the maximum values of  $S$ ,  $S_{\text{max}}$ , and repeat this experiment 1,000 times to calculate the mean of  $S_{\text{max}}$  as a function of  $\bar{n}$ .

Figure 3 shows the result of this experiment. The solid red line shows the approximation to the mean relation,  $S_{\text{th}}(\bar{n})$ , given as  $S_{\text{th}}(\bar{n}) = -0.22\bar{n}^3 + 2.36\bar{n}^2 - 8.37\bar{n} + 15.84$  for  $\bar{n} < 3$  and  $S_{\text{th}}(\bar{n}) = -0.24\bar{n} + 6.74$  for  $\bar{n} \geq 3$ . We note that a typical value of  $\bar{n}$  in the survey fields is 1 to 2, whereas  $\bar{n}$  in GAMA15H is much larger, 7 at  $(m-M)_0 = 18$  and  $\sim 4$  at  $(m-M)_0 \geq 19.5$  because of the presence of the so-called Virgo Overdensity (e.g., Juric et al. 2008). As Figure 3 shows,  $S_{\text{th}}$  ranges from  $\sim 10$  to 7 for  $\bar{n} = 1$  to 2 and  $S_{\text{th}} \simeq 6$  for  $\bar{n} \geq 4$ . The dotted red line in Figure 3 shows  $1.5 \times S_{\text{th}}$ , which lies beyond almost all of the distribution for these purely random fluctuations. Thus, in this work, we adopt the optimal density threshold of  $1.5 \times S_{\text{th}}$  so as to retain promising candidate overdensities from the currently available HSC data.

We have found two candidate overdensities above this detection threshold. The highest signal is from Virgo I ( $S = 12.8$  with  $\bar{n} = 1.87$ ,  $S/S_{\text{th}} = 1.90$ ) as reported in our previous paper (Homma et al. 2016). The second highest signal is found in the direction of Cetus ( $S = 10.7$  with  $\bar{n} = 2.02$ ,  $S/S_{\text{th}} = 1.58$ ). There are other three overdensities with relatively high signal of  $S/S_{\text{th}} = 1.3 \sim 1.4$ , hereafter denoted as overdensities A, B, and C, which however may be false detections as judged from several other properties as explained below.

## 3 Results

Following the procedure described in the previous section, we have found a new satellite candidate in the direction of Cetus, hereafter Cetus III, in addition to Virgo I, and also identified other three overdensities that appear to be false detections. We have also detected known substructures such as known globular clusters, which have a high density signal, which are removed from the following analysis. In this section, we confine ourselves to describe Cetus III in detail and briefly comment on other overdensities showing high signal.



**Fig. 3.** Distribution of the maximum density contrast,  $S_{\max}$ , as a function of  $\bar{n}$  arising from purely random fluctuations in stellar densities (black dots). Solid red line shows the approximation to the mean relation,  $S_{\text{th}}(\bar{n})$ , given as  $S_{\text{th}}(\bar{n}) = -0.22\bar{n}^3 + 2.36\bar{n}^2 - 8.37\bar{n} + 15.84$  for  $\bar{n} < 3$  and  $S_{\text{th}}(\bar{n}) = -0.24\bar{n} + 6.74$  for  $\bar{n} \geq 3$ . Dotted red line shows  $1.5 \times S_{\text{th}}(\bar{n})$ , which is the detection threshold for candidate satellites adopted in this work. Red and blue stars denote Virgo I and Cetus III, respectively, whereas yellow stars denote other three overdensities A, B, and C.

### 3.1 HSC J0209 – 0416 - a new satellite candidate, Cetus III

This overdensity signal with  $S/S_{\text{th}} = 1.58$  and  $\bar{n} = 2.02$  ( $10.7\sigma$ ) is found at  $(\alpha, \delta) = (31^\circ.325, -4^\circ.275)$  and  $(m - M)_0 = 22.0$  mag in the XMM field. Figure 4 shows this feature, which passes the isochrone filter at the above distance modulus, for stars (left) and galaxies (right). It is clear that there is no corresponding overdensity in galaxies.

In Figure 5(a), we plot the spatial distribution of all the stars around this overdensity, which shows a localized concentration of stars within a circle of radius  $2'$ . Panel (b) shows the  $(g - r, r)$  CMD of stars within the  $2'$  radius circle shown in panel (a). This CMD shows a clear signature of a red giant branch (RGB), whereas this feature disappears when we plot stars at  $4' < r < 4'.5$  with the same solid angle, i.e. likely field stars outside the overdensity, as shown in panel (c).

#### 3.1.1 Distance estimate

The heliocentric distance to this stellar system is derived based on the likelihood analysis, for which we use 15 likely member RGBs inside the isochrone envelope in Figure 5(b) inside  $r < 2'$  at the best-fit case of  $(m - M)_0 = 22.0$  in the search of the overdensity. Assuming that the probability distribution,  $P$ , of these member stars relative to the best-fit isochrone in the CMD is Gaussian, we obtain the dependence of  $P$  on  $(m - M)_0$  as shown in Figure 6. We thus arrive at the distance modulus of Cetus III of  $(m - M)_0 = 22.0^{+0.2}_{-0.1}$ , corresponding to the heliocentric distance of  $D = 251^{+24}_{-11}$  kpc.

**Table 1.** Properties of Cetus III

Parameter <sup>a</sup>	Value
Coordinates (J2000)	$31^\circ.331, -4^\circ.270$
Galactic Coordinates ( $l, b$ )	$163^\circ.810, -61^\circ.133$
Position angle	$+101^{+5}_{-6}$ deg
Ellipticity	$0.76^{+0.06}_{-0.08}$
Number of stars, $N_*$	$16^{+3}_{-5}$
$A_V$	0.066 mag
$(m - M)_0$	$22.0^{+0.2}_{-0.1}$ mag
Heliocentric distance	$251^{+24}_{-11}$ kpc
Half light radius, $r_h$	$1'.23^{+0'.42}_{-0'.19}$ or $90^{+42}_{-17}$ pc
$M_{\text{tot}, V}$	$-2.45^{+0.57}_{-0.56}$ mag

<sup>a</sup>Integrated magnitudes are corrected for the mean Galactic foreground extinction,  $A_V$  (Schlafly & Finkbeiner 2011).

#### 3.1.2 Structural parameters

We estimate the structural properties of this overdensity following Martin et al. (2008); Martin et al. (2016). We set six parameters  $(\alpha_0, \delta_0, \theta, \epsilon, r_h, N_*)$ :  $(\alpha_0, \delta_0)$  for the celestial coordinates of the centroid of the overdensity,  $\theta$  for its position angle from north to east,  $\epsilon$  for the ellipticity,  $r_h$  for the half-light radius, and  $N_*$  for the number of stars belonging to the overdensity. The maximum likelihood method of Martin et al. (2008) is applied to the stars within a circle of radius  $8'$  (corresponding to about 5.6 times of the anticipated  $r_h$ ) passing the isochrone filter; the results are summarized in Table 1. It is worth noting that this stellar system is characterized by its small number of stars with  $N_* = 16^{+3}_{-5}$  and ellipticity of  $\epsilon = 0.76$ .

Figure 7 shows the radial profile of the stars passing the isochrone filter [Figure 5(b)] by computing the average density within elliptical annuli. The overplotted line corresponds to the best-fit exponential profile with a half-light radius of  $r_h = 1'.23$  or 90 pc. This spatial size is larger than the typical size of MW globular clusters but is consistent with the scale of dwarf satellites as examined below.

#### 3.1.3 V-band absolute magnitude

The V-band absolute magnitude of Cetus III,  $M_V$ , is estimated in several ways as follows, where for the transformation from  $(g, r)$  to  $V$ , we adopt the formula in Jordi et al. (2006) calibrated for metal-poor Population II stars.

The simplest method is just to sum the luminosities of the stars within the half-light radius,  $r_h$ , and then doubling the summed luminosity (e.g., Sakamoto & Hasegawa 2006). Using the best-fit distance of  $(m - M)_0 = 22.0$  mag, we obtain  $M_V = -3.04^{+0.26}_{-0.39}$  mag for  $r_h = 1'.23^{+0'.42}_{-0'.19}$  and  $(m - M)_0 = 22.0^{+0.2}_{-0.1}$ .

However this method suffers from shot noise due to the small number of stars in Cetus III, which is a significant additional source of uncertainty in estimating  $M_V$ . Thus, as was done in our previous paper (Homma et al. 2016), we adopt a Monte Carlo method similar to that described in Martin et al. (2008) to determine the most likely value of  $M_V$  and its

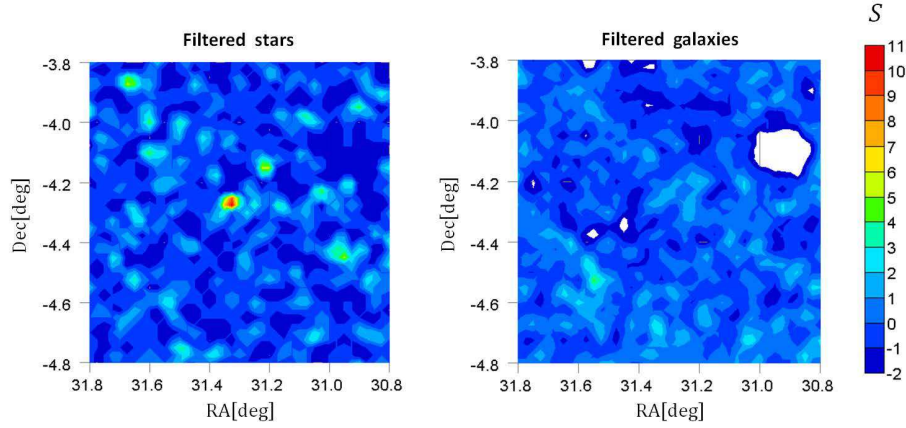


**Fig. 4.** Left panel: the spatial distribution of the stellar overdensity in Cetus passing the isochrone filter at  $(m - M)_0 = 22.0$  with constraints of  $i < 24.5$  and  $g - r < 1.0$ , covering one square degree centered on this candidate. Right panel: the plot for the sources classified as galaxies passing the same isochrone filter and same constraints as for the stars in the left panel. Note that there is no overdensity at the center of this plot.

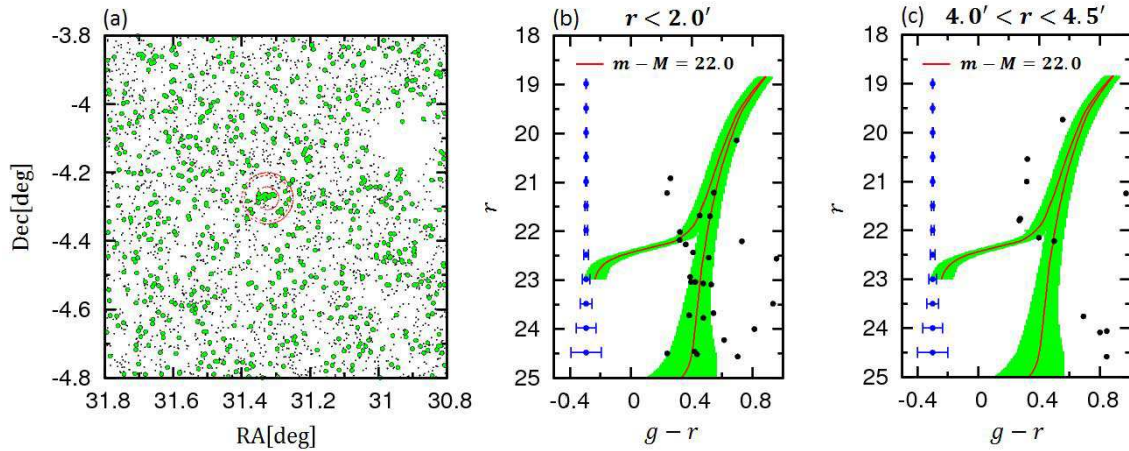


**Fig. 5.** Panel (a): the spatial distribution of the stars around the overdensity in Cetus, where green circles (black dots) denote the stars inside (outside) the isochrone filter at  $(m - M)_0 = 22.0$ . Red circles denote annuli with radii  $r = 2'$ ,  $4'$ , and  $4'.5$  from the center. Panel (b): the distribution of the stars in the  $g - r$  vs.  $r$  CMD at  $r < 2'$ . Panel (c): the same as (b) but for field stars at  $4' < r < 4'.5$ , which has the same solid angle. Note the absence of a red giant branch.

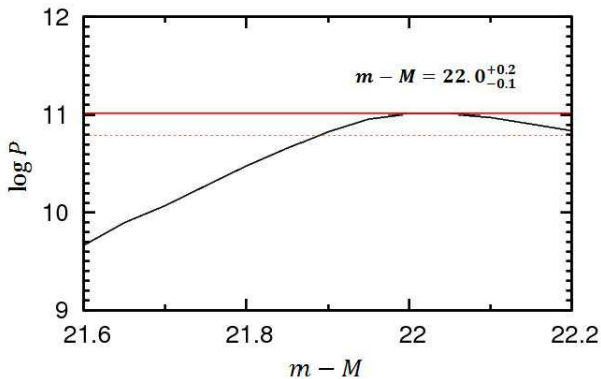


**Fig. 6.** Probability distribution of the 15 likely member stars at  $r < 2'$  relative to the best-fit isochrone case at  $(m - M)_0 = 22.0$  as a function of  $(m - M)_0$ . The maximum probability is  $\log P = 11.01$  delineated with red solid line and  $1\sigma$  interval is denoted by red dotted line.

uncertainty. Based on the values of  $N_* = 16_{-5}^{+3}$  at  $i < 24.5$  mag and  $(m - M)_0 = 22.0_{-0.1}^{+0.2}$  mag obtained in the previous subsection and on a stellar population model with an age of 13 Gyr and metallicity of  $[M/H] = -2.2$ , we generate  $10^4$  realizations of CMDs for the initial mass function (IMF) by Kroupa (2002). We then derive the luminosity of the stars at  $i < 24.5$  mag, taking into account the completeness of the observed stars with HSC. The median (mean) value of  $M_V$  is then given as  $M_V = -2.45_{-0.56}^{+0.57}$  mag ( $M_V = -2.58_{-0.34}^{+0.69}$  mag). When we consider unobserved faint stars below the limit of  $i = 24.5$ , the  $M_V$  estimate becomes slightly brighter,  $M_V = -3.09_{-0.44}^{+0.57}$  mag ( $M_V = -3.14_{-0.34}^{+0.49}$  mag). Note that all of these  $M_V$  values are consistent within the  $1\sigma$  uncertainty and also are insensitive to the adoption of different IMFs such as Salpeter and Chabrier IMFs (Salpeter 1995; Chabrier 2001).

In deriving  $M_V$  corrected for unobserved faint stars, we are also able to obtain the total mass of stars in

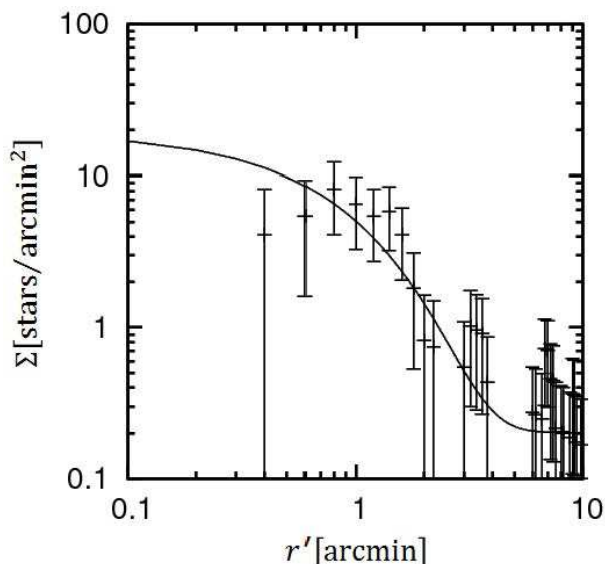


Fig. 7. Density profile of the stars in Cetus III that pass the isochrone filter shown in Figure 5(b), in elliptical annuli as a function of mean radius, where the uncertainties are derived assuming Poisson statistics. The line shows a fitted exponential profile with  $r_h = 1'.23$ .

Table 2. Revised Properties of Virgo I

Parameter <sup>a</sup>	Value
Coordinates (J2000)	180°.038, -0°.681
Galactic Coordinates ( $l, b$ )	276°.942, +59°.578
Position angle	+62 <sup>+8</sup> <sub>-13</sub> deg
Ellipticity	0.59 <sup>+0.12</sup> <sub>-0.14</sub>
Number of stars, $N_*$	18 <sup>+5</sup> <sub>-4</sub>
$A_V$	0.066 mag
$(m - M)_0$	19.8 <sup>+0.2</sup> <sub>-0.1</sub> mag
Heliocentric distance	91 <sup>+9</sup> <sub>-4</sub> kpc
Half light radius, $r_h$	1'.76 <sup>+0'.49</sup> <sub>-0'.40</sub> or 47 <sup>+19</sup> <sub>-13</sub> pc
$M_{\text{tot},V}$	-0.33 <sup>+0.75</sup> <sub>-0.87</sub> mag

<sup>a</sup> Integrated magnitudes are corrected for the mean Galactic foreground extinction,  $A_V$  (Schlafly & Finkbeiner 2011).

Cetus III,  $M_*$ , for different IMFs. They are summarized as  $M_* = 2300^{+917}_{-785} M_\odot$  (Kroupa),  $4302^{+1833}_{-1721} M_\odot$  (Salpeter), and  $2205^{+894}_{-771} M_\odot$  (Chabrier).

## 3.2 Properties of other overdensities showing high signal

### 3.2.1 HSC J1200 – 0040 - Virgo I

This new satellite already reported in Homma et al. (2016) shows the highest signal of  $S = 12.8$  with  $\bar{n} = 1.87$  and  $S/S_{\text{th}} = 1.90$ . In contrast to our previous paper (Homma et al. 2016), we have adopted the  $i$ -band data for the removal of contaminations in addition to the  $g$  and  $r$ -band data, so that the final results for the physical parameters of stellar system are slightly changed. We thus list the revised values for Virgo I in Table 2, although the differences are well within the  $1\sigma$  uncertainty. For the median (mean) value of  $M_V$  with completeness correction,

we obtain  $M_V = -0.33^{+0.75}_{-0.87}$  mag ( $M_V = -0.76^{+1.18}_{-0.45}$  mag)<sup>1</sup>. When we correct for unobserved faint stars below the limit of  $i = 24.5$ , we obtain  $M_V = -0.70^{+0.55}_{-0.69}$  mag ( $M_V = -1.04^{+0.80}_{-0.38}$  mag). The total stellar mass of Virgo I is estimated as  $M_* = 323^{+129}_{-108} M_\odot$  (Kroupa),  $625^{+255}_{-211} M_\odot$  (Salpeter), and  $313^{+128}_{-101} M_\odot$  (Chabrier).

### 3.2.2 Other three high signals with possibly false detections

We summarize the status of the other three overdensities, A, B, and C, found from their relatively high signals of  $S/S_{\text{th}}$ . They are plotted in Figure 8, 9 and 10.

- A: (RA,DEC) = (239°.200, 43°.725) (in HECTOMAP) at  $(m - M)_0 = 17.5$  giving  $S/S_{\text{th}} = 1.39$  with  $\bar{n} = 1.40$  (Figure 8): the paucity of main-sequence stars even at  $r < 2'$  makes it difficult to conclude that this overdensity is a stellar system.
- B: (RA,DEC) = (242°.800, 43°.475) (in HECTOMAP) at  $(m - M)_0 = 24.0$  giving  $S/S_{\text{th}} = 1.33$  with  $\bar{n} = 1.44$  (Figure 9): this somewhat high signal is given only by the effect of a few stars in the bright RGB locus at  $r < 2'$ . It is thus difficult to conclude robustly that this feature is the signature of a stellar system. Deeper imaging with space telescopes would be worthwhile for trying to identify fainter RGB stars against background faint galaxies.
- C: (RA,DEC) = (16°.100, -0°.750) (in WIDE01H) at  $(m - M)_0 = 17.0$  giving  $S/S_{\text{th}} = 1.41$  with  $\bar{n} = 2.07$  (Figure 10): since this field still lacks data in  $i$  band, the removal of background galaxies based on the color cut is incomplete. The CMD at  $r < 2'$  also implies that the signal is due to the contamination of galaxies.

## 4 Discussion

### 4.1 Comparison with globular clusters and other satellites

Figure 11(a) shows the comparison in the size and absolute magnitude of the stellar system, measured by  $r_h$ , between MW globular clusters (dots) (Harris 1996) and the known dwarf satellites (squares) (McConnachie 2012; Bechtol et al. 2015; Koposov et al. 2015; Drlica-Wagner et al. 2015; Laevens et al. 2014; Kim et al. 2015; Kim & Jerjen 2015; Laevens et al. 2015a; Laevens et al. 2015b) including recent discoveries of the DES and PS1 surveys. Red and blue squares with error bars show Virgo I and Cetus III, respectively.

Both Cetus III and Virgo I are significantly larger than MW globular clusters with comparable  $M_V$ . They both are located along the locus of MW dwarf satellites, thereby suggesting that Cetus III is a new ultra-faint dwarf galaxy. This stellar system is significantly flattened with an ellipticity of  $\epsilon = 0.76^{+0.06}_{-0.08}$  like UMa I with  $\epsilon = 0.80$  (Martin et al. 2008), which also supports

<sup>1</sup> In Homma et al. (2016), we reported only the mean  $M_V$  of  $\sim -0.8$  mag.

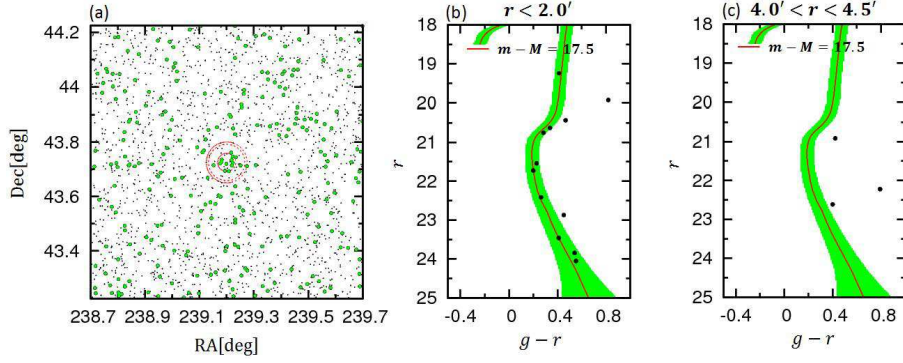


**Fig. 8.** Panel (a): the spatial distribution of stars in the overdensity A with  $S/S_{\text{th}} = 1.39$  found at (RA,DEC) =  $(239^\circ.200, 43^\circ.725)$ , where red circles denote annuli with radii  $r = 2'$ ,  $4'$ , and  $4'.5$  from the center. Panel (b): the distribution of the stars in the  $g-r$  vs.  $r$  CMD at  $r < 2'$ . Panel (c): the same as (b) but for field stars at  $4' < r < 4'.5$ .

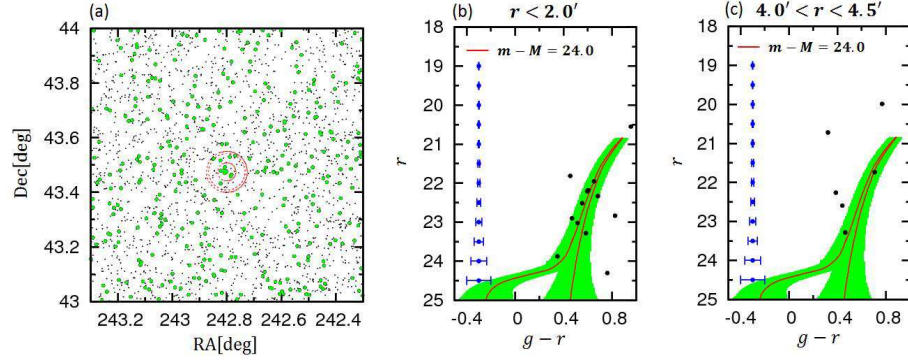


**Fig. 9.** The same as Figure 8 but for the overdensity B with  $S/S_{\text{th}} = 1.33$  found at (RA,DEC) =  $(242^\circ.800, 43^\circ.475)$ .

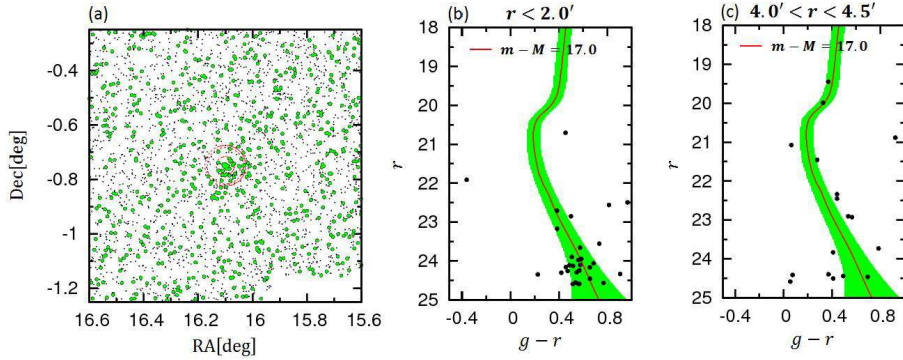


**Fig. 10.** The same as Figure 8 but for the overdensity C with  $S/S_{\text{th}} = 1.41$  found at (RA,DEC) =  $(16^\circ.100, -0^\circ.750)$ .

this conclusion.

Figure 11(b) shows the relation between  $M_V$  and the heliocentric distance for MW globular clusters and dwarf satellites including Virgo I and Cetus III. Red and blue lines denote the detection limits of SDSS and HSC, respectively. As is clear, both Cetus III at  $251_{-11}^{+24}$  kpc and Virgo I at  $91_{-4}^{+9}$  kpc are well beyond the detection limit of SDSS and are close to the limit of HSC.

## 4.2 Implication for the missing satellites problem

We have identified two new dwarf satellites from  $\sim 300 \text{ deg}^2$  of HSC data in the outer part of the MW halo, where no other survey programs can reach. This suggests that we can expect to find more dwarf satellites within the detection limit of HSC as the survey footprint grows. In order to assess if this is consistent with the prediction of  $\Lambda$ CDM models in the context of the missing satellites problem, and determine how many more satellites will be found in the completed HSC survey over  $\sim 1400 \text{ deg}^2$ , we examine the recent results of high-resolution N-body simulation for  $\Lambda$ CDM models and estimate the most likely number

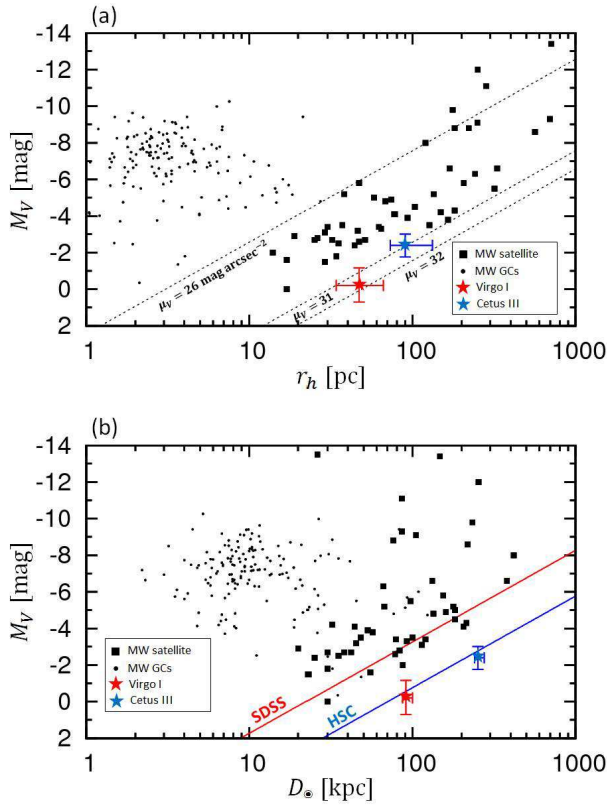


**Fig. 11.** (a) The relation between  $M_V$  and  $r_h$  for stellar systems. Dots denote globular clusters in the MW taken from Harris (1996). Filled squares denote the MW dSphs taken from McConnachie (2012), the recent DES work for new ultra-faint MW dSphs (Bechtol et al. 2015; Koposov et al. 2015; Drlica-Wagner et al. 2015), and other recent discoveries (Laevens et al. 2014; Kim et al. 2015; Kim & Jerjen 2015; Laevens et al. 2015a; Laevens et al. 2015b). The red and blue stars with error bars correspond to Virgo I and Cetus III, respectively, both of which lie within the locus defined by dSphs. The dotted lines indicate the constant surface brightness,  $\mu_V = 26, 31,$  and  $32$  mag arcsec $^{-2}$ . (b) The relation between  $M_V$  and heliocentric distance for the systems shown in panel (a). The red and blue lines indicate the detection limits of SDSS and HSC, respectively.

of visible satellites with HSC based on several assumptions for the baryon fraction relative to dark matter and the spatial distribution of dark halos.

First, to derive the mass function of subhalos associated with a MW-sized host halo, we adopt the result of the Caterpillar simulation (Griffen et al. 2016) for the cosmological evolution of cold dark matter halos (Dooley et al. 2016). The Caterpillar simulation is suitable for our current purpose because of its very high mass resolution of  $\sim 10^4 M_\odot$ /particle designed to study the properties of subhalos. We adopt the analysis of this simulation by Dooley et al. (2016) in what follows. The mass function of subhalos with mass  $M_{\text{sub}}$  associated with a MW-sized host halo with mass  $M_{\text{host}}$  is given as

$$\frac{d\bar{N}}{dM_{\text{sub}}} = K_0 \left( \frac{M_{\text{sub}}}{M_\odot} \right)^{-\alpha} \frac{M_{\text{host}}}{M_\odot}, \quad (2)$$

where we adopt  $K_0 = 0.00188$ ,  $\alpha = 1.87$ , and  $M_{\text{host}} = 1.4 \times$

$10^{12} M_\odot$  in what follows.

Here, the number of simulated subhalos varies with the distance,  $r$ , from the center of a host halo. The cumulative number of subhalos inside  $r$  in the Caterpillar simulation is obtained from Equation (2) by multiplying by the fraction of subhalos within a radius  $r$ , as  $f_{\text{sub}}(< r)$ , parameterized  $f_{\text{sub}}(< r) = k_1 + k_2(r/R_{\text{vir}}) + k_3(r/R_{\text{vir}})^2 + k_4(r/R_{\text{vir}})^3$  with  $(k_1, k_2, k_3, k_4) = (-0.0440, 0.3913, 0.9965, -0.3438)$  (Dooley et al. 2016). We ignore the effect of any anisotropic distribution of subhalos; no anisotropy is seen in the Caterpillar simulation.

Second, based on this mass function of subhalos, we estimate the likely stellar mass function using the abundance matching method for assigning stellar mass  $M_*$  to a dark halo with mass  $M_{\text{halo}}$ . We follow the paper by Garrison-Kimmel et al. (2017), in which the  $M_*$  vs.  $M_{\text{halo}}$  relation derived from the massive regime  $M_{\text{halo}} > 10^{11.5} M_\odot$  ( $M_* > 5 \times 10^9 M_\odot$ ) is extrapolated to the lower masses with finite scatter<sup>2</sup>. We adopt a larger scatter with decreasing  $M_{\text{halo}}$  in this lower mass range, parameterized by  $v = -0.2$  in their formulation [See equation (3) of Garrison-Kimmel et al. (2017)]. With this, the corresponding luminosity function of satellites,  $d\bar{N}/dM_V$ , can be inferred once the mass to light ratio,  $\Upsilon_*$ , is given. The cumulative luminosity function of subhalos derived in this way is shown in Figure 12 (black solid line), where we assume  $\Upsilon_* = 2$  in solar units. This plot suggests the presence of  $\sim 1000$  visible satellites with  $M_V < 0.0$  in a MW-sized halo.

Given the theoretically predicted number of visible satellites from  $\Lambda$ CDM models, we consider the specific settings of HSC-SSP in its survey area and depth to estimate the actual number of observable satellites, following the work by Tollerud et al. (2008) estimated for SDSS.

First, HSC-SSP in its Wide layer will observe a fraction of the sky  $f_{\Omega, \text{HSC}} = (1400 \text{ deg}^2 / 41252 \text{ deg}^2) = 0.034$ . Next, we consider the completeness correction due to the detection limit of HSC,  $f_{r, \text{HSC}}$ , which thus depends on  $M_V$ . To do so, we use a spherical completeness radius,  $R_{\text{comp}}^{\text{SDSS}}(M_V)$ , derived for SDSS, beyond which a satellite of a particular magnitude is undetected (Tollerud et al. 2008),

$$R_{\text{comp}}^{\text{SDSS}}(M_V) = \left( \frac{3}{4\pi f_{\text{DR5}}} \right)^{1/3} 10^{(-aM_r - b)/3} \text{ Mpc}, \quad (3)$$

where  $f_{\text{DR5}} = 0.194$  is the sky coverage of SDSS DR5 and  $(a, b)$  depends on the assumed value of a virial radius. The corresponding radius for HSC,  $R_{\text{comp}}^{\text{HSC}}$ , is given as

$$R_{\text{comp}}^{\text{HSC}} / R_{\text{comp}}^{\text{SDSS}}(M_V) = 10^{(M_{r, \text{HSC}} - M_{r, \text{SDSS}})/5}, \quad (4)$$

where  $M_{r, \text{HSC}}$  and  $M_{r, \text{SDSS}}$  are cut-off  $r$ -band magnitudes for HSC and SDSS, respectively. We set  $M_{r, \text{SDSS}} = 22.2$  mag with  $\sim 100\%$  completeness and  $M_{r, \text{HSC}} = 24.7$  mag with  $\sim 50\%$

<sup>2</sup> In Garrison-Kimmel et al. (2017),  $M_{\text{halo}}$  is defined as the largest instantaneous virial mass associated with the main branch of each subhalo's merger tree, and we follow this definition in our analysis.

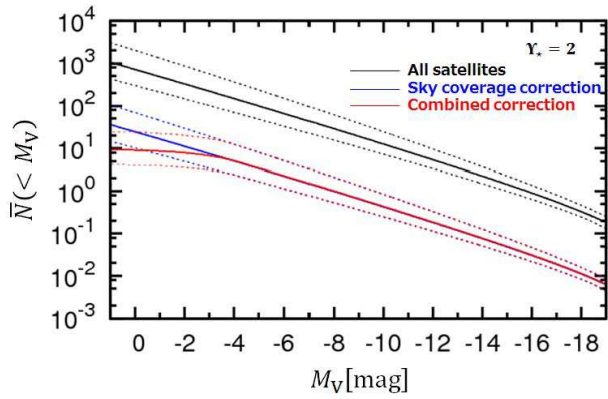


**Fig. 12.** Black solid line denotes the cumulative luminosity function of visible satellites calculated from subhalos in a MW-sized halo taken from Caterpillar simulation, where we assume the mass to light ratio of  $\Upsilon_* = 2$ . Blue solid line considers the correction only for the sky coverage,  $f_{\Omega, \text{HSC}}$ , of the HSC-SSP survey, whereas red solid line considers all the corrections associated with the HSC-SSP survey as given in Equation (6). Dotted lines above and below all of black, green and red solid lines correspond to typical errors associated with the abundance matching method for transforming dark-halo mass to stellar mass.

completeness, since the cut-off magnitude in  $i$  in this work is  $i = 24.5$  mag and typical satellite stars show  $r - i = 0.2$ . We thus obtain

$$f_{r, \text{HSC}}(M_V) = f_{\text{sub}}(< R_{\text{comp}}^{\text{SDSS}}(M_V)), \quad (5)$$

where we set  $R_{\text{vir}} = 417$  kpc so as to include Leo T and set  $a$  and  $b$  in equation (3) to (0.684, 5.667) (Tollerud et al. 2008). We then derive the cumulative luminosity function of satellites observable by HSC-SSP, as

$$\frac{d\bar{N}_{\text{HSC}}}{dM_V} = f_{\Omega, \text{HSC}} f_{r, \text{HSC}}(M_V) \frac{d\bar{N}}{dM_V}. \quad (6)$$

In Figure 12, the blue solid line corresponds to the luminosity function corrected only for the sky coverage,  $f_{\Omega, \text{HSC}}$ , and the red solid line considers the full correction given in equation (6), i.e., the expected number of satellites in the HSC-SSP survey. We assume here  $\Upsilon_* = 2$ , but even if we adopt  $\Upsilon_* = 1$  or 4, the number of satellites is within the uncertainty of the abundance matching method shown with dotted lines in Figure 12.

Although there remain uncertainties in the prediction of visible satellites, we anticipate that the completed 1,400 deg<sup>2</sup> HSC-SSP survey will find  $9_{-5}^{+15}$  satellites with  $M_V < 0.0$ . Thus far, we have identified two new satellites over  $\sim 300$  deg<sup>2</sup>, which is consistent with this prediction. Thus, further search for new satellites from HSC-SSP survey will provide important insights into the missing satellites problem.

## 5 Conclusions

In this paper, we have presented our updated method, compared to our previous work (Homma et al. 2016), for the systematic search for old stellar systems from 300 deg<sup>2</sup> of HSC-SSP

survey data and have identified a new ultra-faint dwarf satellite, Cetus III, as a statistically high overdensity, in addition to Virgo I. This stellar system is a  $10.7\sigma$  overdensity in the relevant isochrone filter in the relevant survey area. Based on a maximum likelihood analysis, the half-light radius of Cetus III is estimated to be  $\sim 90$  pc. This is significantly larger than MW globular clusters with the same luminosity of  $M_V \sim -2.5$  mag, thereby suggesting that it is a dwarf galaxy. Deeper imaging of Cetus III with space telescopes will be worthwhile for getting further constraints from its faint RGB/MS members against background faint galaxies. Also, spectroscopic follow-up studies of stars in Cetus III will be important to constrain their membership and determine chemical abundance and stellar kinematics, so that chemo-dynamical properties of this satellite may be derived and compared to other satellites.

The heliocentric distance to Cetus III is  $251_{-11}^{+24}$  kpc or  $(m - M)_0 = 22.0_{-0.1}^{+0.2}$  mag and its completeness-corrected, absolute magnitude in the  $V$  band is estimated as  $M_V = -2.45_{-0.56}^{+0.57}$  mag. This suggests that Cetus III lies beyond the reach of the SDSS but inside the detection limit of the HSC-SSP survey, for which we adopt the limiting  $i$ -band magnitude of 24.5 mag below which star/galaxy classification becomes difficult. Thus, we expect the presence of more satellites in the MW halo, which have not yet been identified because of their faint luminosities and large distances. Based on the results of high-resolution N-body simulations for the evolution of dark matter halos combined with the abundance matching method to derive stellar masses, we have calculated the luminosity function of visible satellites associated with numerous subhalos in a MW-sized host halo to estimate the likely number of new dwarf satellites to be discovered in the Subaru/HSC survey. Although this estimate suffers from uncertainties mainly from the abundance matching method, we anticipate that we will discover  $9_{-5}^{+15}$  satellites with  $M_V < 0$  in the HSC-SSP survey volume. Therefore the completion of this survey program will provide important insights into the missing satellites problem and thus the nature of dark matter on small scales.

## Acknowledgments

This work is based on data collected at the Subaru Telescope and retrieved from the HSC data archive system, which is operated by Subaru Telescope and Astronomy Data Center at National Astronomical Observatory of Japan. MC acknowledges support in part from MEXT Grant-in-Aid for Scientific Research on Innovative Areas (No. 15H05889, 16H01086).

The Hyper Suprime-Cam (HSC) collaboration includes the astronomical communities of Japan and Taiwan, and Princeton University. The HSC instrumentation and software were developed by the National Astronomical Observatory of Japan (NAOJ), the Kavli Institute for the Physics and Mathematics of the Universe (Kavli IPMU), the University of Tokyo, the High Energy Accelerator Research Organization (KEK), the Academia Sinica Institute for Astronomy and Astrophysics in Taiwan (ASIAA), and Princeton University. Funding was contributed by the

FIRST program from Japanese Cabinet Office, the Ministry of Education, Culture, Sports, Science and Technology (MEXT), the Japan Society for the Promotion of Science (JSPS), Japan Science and Technology Agency (JST), the Toray Science Foundation, NAOJ, Kavli IPMU, KEK, ASIAA, and Princeton University.

This paper makes use of software developed for the Large Synoptic Survey Telescope. We thank the LSST Project for making their code available as free software at <http://dm.lsst.org>.

The Pan-STARRS1 Surveys (PS1) have been made possible through contributions of the Institute for Astronomy, the University of Hawaii, the Pan-STARRS Project Office, the Max-Planck Society and its participating institutes, the Max Planck Institute for Astronomy, Heidelberg and the Max Planck Institute for Extraterrestrial Physics, Garching, The Johns Hopkins University, Durham University, the University of Edinburgh, Queen's University Belfast, the Harvard-Smithsonian Center for Astrophysics, the Las Cumbres Observatory Global Telescope Network Incorporated, the National Central University of Taiwan, the Space Telescope Science Institute, the National Aeronautics and Space Administration under Grant No. NNX08AR22G issued through the Planetary Science Division of the NASA Science Mission Directorate, the National Science Foundation under Grant No. AST-1238877, the University of Maryland, and Eotvos Lorand University (ELTE) and the Los Alamos National Laboratory.

## References

- Abazajian, K., Adelman-McCarthy, J. K., Agüeros, M. A., et al. 2004, *AJ*, 128, 502
- Abbott, T., Abdalla, F. B., Allam, S., et al. 2016, *MNRAS*, in press (arXiv:1601.00329)
- Aihara, H., Armstrong, R., Bickerton, S., et al. 2017a, arXiv:1702.08449 (HSC DR1 paper)
- Aihara, H., Arimoto, N., Armstrong, R., et al. 2017b, (HSC overview and survey paper)
- Axelrod, T., Kantor, J., Lupton, R. H., & Pierfederici, F. 2010, in Proc. SPIE, Vol. 7740, Software and Cyberinfrastructure for Astronomy, 774015
- Bechtol, K., Drlica-Wagner, A., Balbinot, E., et al. ApJ, 807, 50
- Belokurov, V., Zucker, D. B., Evans, N. W., et al. 2006, *ApJL*, 647, L11
- Bosch, J. et al. 2017, PASJ, to be submitted
- Boylan-Kolchin, M., Bullock, J. S., Kaplinghat, M. 2011, *MNRAS*, 415, L40
- Boylan-Kolchin, M., Bullock, J. S., Kaplinghat, M. 2012, *MNRAS*, 422, 1203
- Bressan, A., Marigo, P., Girardi, L., et al. 2012, *MNRAS*, 427, 127
- Burkert, A. 1995, *ApJ*, 447, L25
- Chabrier, G., 2001, *ApJ*, 554, 1274
- Chambers, K. C., et al. 2016, arXiv: 1612.05560
- de Blok, W. J. G., McGaugh, S. S., Bosma, A., & Rubin, V. C. 2001, *ApJ*, 552, L23
- Dooley, G. A., Peter, A. H. G., Yang, T., et al. 2016, arXiv:1610.00708
- Drlica-Wagner, A., Bechtol, K., Rykoff, E. S., et al. 2015, *ApJ*, 813, 109
- Garrison-Kimmel, S., Bullock, J. S., Boylan-Kolchin, M., & Bardwell, E. 2017, *MNRAS*, 464, 3108
- Gilmore, G., Wilkinson, M. I., Wyse, R. F. G., et al. 2007, *ApJ*, 663, 948
- Griffen, B. F., Ji, A. P., Dooley, G. A., et al. 2016, *ApJ*, 818, 10
- Gunn, J. E., & Stryker, L. L., 1983, *ApJS*, 52, 121
- Harris, W. E. 1996, *AJ*, 112, 1487
- Homma, D., Chiba, M., Okamoto, S., et al. 2016, *ApJ*, 832, 21
- Ibata, R. A., Lewis, G. F., Conn, A. R., et al. 2013, *Nature*, 493, 62
- Ivezić, Z., Axelrod, T., Brandt, W. N., et al. 2008, *AJ*, 176, 1
- Jordi, K., Grebel, E. K., Ammon, K. 2006, *aj*, 460, 339
- Juric, M., Ivezić, Z., Brooks, A., et al. 2008, *ApJ*, 673, 864
- Juric, M., Kantor, J., Lim, K.-T., et al. 2015, *ArXiv e-prints*, arXiv:1512.07914
- Kim, D., Jerjen, H., Milone, A. P. et al. 2015, *ApJ*, 803, 63
- Kim, D., & Jerjen, H. 2015, *ApJ*, 808, L39
- Klypin, A., Kravtsov, A. V., Valenzuela, O., & Prada, F. 1999, *ApJ*, 522, 82
- Koposov, S., Belokurov, V., Evans, N. W., et al. 2008, *ApJ*, 686, 279
- Koposov, S. E., Belokurov, V., Torrealba, G., & Evans, N. W. 2015, *ApJ*, 805, 130
- Kroupa, P., 2002, *Science*, 295, 82
- Kroupa, P., Theis, C., & Boily, C. M. 2005, *A&A*, 431, 517
- Laevens, B. P. M., Martin, N. F., Sesar, B., et al. 2014, *ApJL*, 786, L3
- Laevens, B. P. M., Martin, N. F., Ibata, R. A. et al. 2015a, *ApJL*, 802, L18
- Laevens, B. P. M., Martin, N. F., Bernard, E. J. et al. 2015b, *ApJL*, 813, L44
- Leauthaud, A., Massey, R., Kneib, J.-P., et al. 2007, *ApJS*, 172, 219
- Macciò, A. V., & Fontanot, F. 2010, *MNRAS*, 404, L16
- Magnier, E. A., Schlafly, E., Finkbeiner, D., et al. 2013, *ApJS*, 205, 20
- Martin, N. F., de Jong, J. T. A., & Rix, H.-W. 2008, *ApJ*, 684, 1075
- Martin, N. F., Ibata, R. A., Lewis, G. F., et al. 2016, *ApJ*, 833, 167
- McConnachie, A. W., & Irwin, M. J. 2006, *MNRAS*, 365, 902
- McConnachie, A. W., 2012, *AJ*, 144, 4
- Milosavljević, M., & Bromm, V. 2014, *MNRAS*, 440, 50
- Miyazaki, S., Komiyama, Y., Nakata, H., et al. 2012, *Proc. SPIE*, 8446, 84460Z
- Miyazaki, S., et al. 2017, PASJ, to be submitted
- Moore, B., 1994, *Nature*, 370, 629
- Moore, B., Ghigna, S., Governato, F., Lake, G., Quinn, T., & Stadel, J. 1999, *ApJL*, 524, L19
- Oh, S.-H., de Blok, W. J. G., Brinks, E., Walter, F., & Kennicutt, Jr., R. C. 2011, *AJ*, 141, 193
- Okayasu, Y., & Chiba, M. 2016, *ApJ*, 827, 105
- Pawlowski, M. S., Pflamm-Altenburg, J., & Kroupa, P. 2012, *MNRAS*, 423, 1109
- Pawlowski, M. S., Kroupa, P., & Jerjen, H. 2013, *MNRAS*, 435, 1928
- Pawlowski, M. S., Famaey, B., Merritt, D., & Kroupa, P. 2015, *ApJ*, 815, 19
- Sakamoto, T., & Hasegawa, T. 2006, *ApJ*, 653, L29
- Salpeter, E. E. 1955, *ApJ*, 121, 161
- Sawala, T., Frenk, C. S., & Fattahi, A., et al. 2016, *MNRAS*, 457, 1931
- Schlafly, E. F., & Finkbeiner, D. P. 2011, *ApJ*, 737, 103
- Schlafly, E. F., Finkbeiner, D. P., Jurić, M., et al. 2012, *ApJ*, 756, 158
- Schlegel, D. J., Finkbeiner, D. P., & Davis, M. 1998, *ApJ*, 500, 525
- Simon, J. D., & Geha, M. 2007, *ApJ*, 670, 313
- Swaters, R. A., Madore, B. F., van den Bosch, F. C., & Balcells, M. 2003, *ApJ*, 583, 732
- Tegmark, M. et al., 2004, *ApJ*, 606, 702
- Tollerud, E. J., Bullock, J. S., Strigari, L. E., & Willman, B. 2008, *ApJ*, 688, 277
- Tonry, J. L., Stubbs, C. W., Lykke, K. R., et al. 2012, *ApJ*, 750, 99
- Walsh, S. M., Willman, B., & Jerjen, H. 2009, *AJ*, 137, 45
- Willman, B., Dalcanton, J., Ivezić, Z. et al. 2002, *AJ*, 123, 848
- Willman, B., Blanton, M. R., West, A. A., et al. 2005, *AJ*, 129, 2692

York, D. G., Adelman, J., Anderson, J. E., Jr., et al. 2000, *AJ*, 120, 1579